

Formation of matter-wave soliton trains by modulational instability

Jason H.V. Nguyen, De Luo, and Randall G. Hulet*

Department of Physics and Astronomy, Rice University, Houston TX, 77005, USA

*To whom correspondence should be addressed; E-mail: randy@rice.edu.

Nonlinear systems can exhibit a rich set of dynamics that are inherently sensitive to their initial conditions. One such example is modulational instability, which is believed to be one of the most prevalent instabilities in nature. By exploiting a shallow zero-crossing of a Feshbach resonance, we characterize modulational instability and its role in the formation of matter-wave soliton trains from a Bose-Einstein condensate. We examine the universal scaling laws exhibited by the system and, through real-time imaging, address a long-standing question of whether the solitons in trains are created with effectively repulsive nearest-neighbor interactions or rather evolve into such a structure.

Modulational instability (MI) is a process in which broadband perturbations spontaneously seed the nonlinear growth of a nearly monochromatic wave disturbance (*1*). Owing to its generality, MI plays a role in a variety of different physical systems such as water waves, where it is known as a Benjamin-Feir instability (*2*); plasma waves; nonlinear optics (*3–5*); and ultracold atomic gases (*6*). The nonlinear interaction resulting in MI also supports solitons, which are localized waves whose dispersion is exactly balanced by the nonlinearity (*7, 8*). Thus, the rapid

growth of fluctuations from MI, which leads to the breakup of the wave, is seen as a natural precursor to the formation of soliton trains. In optical systems, this was first observed in the temporal domain (9–11) and, subsequently, in the spatial domain (12).

Analogously, in an atomic Bose-Einstein condensate (BEC), MI drives the spontaneous formation of bright matter-wave solitons when the interaction between atoms is rapidly quenched from repulsive to attractive. These systems are well described in most respects by the Gross-Pitaevskii equation, which is equivalent to the nonlinear Schrödinger equation with the addition of a harmonic trapping potential. Here, the nonlinearity is determined by the s-wave scattering length, which is positive for a repulsive, defocusing nonlinearity and negative for an attractive, focusing one. We will see that dissipation plays an important role in the matter-wave system, as it does in optical media.

Bright matter-wave solitons were first observed by applying an interaction ramp traversing a zero-crossing of the interaction parameter in a quasi-one-dimensional (quasi-1D) BEC (13, 14). Several experiments have produced trains of up to 10 solitons (14, 15). Because these solitons are harmonically confined they are not truly 1D and are susceptible to collapse resulting from the attractive nonlinearity. This has the effect of limiting the number of atoms a single soliton can stably support (16–18). Additionally, solitons themselves may interact, exhibiting an effectively attractive or repulsive force that, according to mean-field theory, can be ascribed to a relative phase between solitons of $\Delta\phi \approx 0$ or $\Delta\phi \approx \pi$, respectively (19). These phase-dependent interactions were first observed in optical solitons (20, 21). In the case of matter-wave solitons, the peak density increases for in-phase collisions ($\Delta\phi \approx 0$) which can produce annihilations and mergers, whereas out-of-phase collisions ($\Delta\phi \approx \pi$) are expected to be more stable against collapse (22–25). These effects have been observed experimentally (26). Solitons created in trains were found to be surprisingly stable, persisting for many cycles of oscillation in a harmonic trap despite being near the threshold for collapse (14, 15). From this observation, it was

inferred that an alternating-phase ($0-\pi-0$) structure was present, protecting the structure against collapse (14, 15). Detailed theoretical investigations have studied the formation of matter-wave soliton trains and attempted to explain the origins of the observed repulsive interaction between neighboring solitons (25, 27–33). We address these issues in the experiments described here.

For MI, there is a positive feedback-driven exponential growth that is largest for the wavenumber $k_{MI} = \sqrt{4|a_f|n_{1D}/a_r}$ (29, 30). Here, $a_r = \sqrt{\hbar/(m\omega_r)}$ is the characteristic confinement length in the radial direction, \hbar is Planck’s constant divided by 2π , m is the atomic mass, ω_r is the radial frequency of the harmonic trap, a_f is the (negative) scattering length after the quench, and n_{1D} is the line density of the condensate before the quench. The healing length, $\xi = k_{MI}^{-1}$, naturally lends itself as the characteristic length scale for MI in this system; correspondingly, the rate at which fluctuations grow sets a characteristic time scale given by γ^{-1} , where $\gamma = \hbar k_{MI}^2/(2m)$.

Once the scattering length is quenched from positive to negative, the effects of MI manifest as density modulations of the gas (Fig. 1A). The atoms first clump together into regions of increased density, owing to the nonlinear focusing of the attractive interaction. Regions of high density, separated by a spatial distance of $2\pi\xi$ appear on a timescale given by γ^{-1} . These density clumps evolve into solitons whose dispersion is balanced by the nonlinear attraction between atoms.

Although it is clear that MI is crucial to the formation of matter-wave soliton trains (27–32), the identification of the mechanism responsible for their stability has remained elusive. Several theories have been proposed. In the simulations of Ref. 27, the authors determined the spectrum of the phase of the wavefunction produced by quantum fluctuations when the scattering length was suddenly quenched. They imprinted the condensate wavefunction with this phase and found the subsequent development of an alternating phase structure and dynamics that match those of the experiment (14).

In another study (28), similar dynamics were calculated with the use of an effective time-dependent 1D nonpolynomial Schrödinger equation, but an alternating phase structure was simply imprinted onto the solitons. In a subsequent paper (29), imprinting the condensate with an ad hoc phase structure was shown to be unnecessary; a nearly alternating-phase structure emerged in numerical simulations by allowing the phase of the condensate to evolve self-consistently according to a Gross-Pitaevskii equation that included a dissipative three-body term.

In Ref. 30, self-interference, rather than quantum fluctuations served to seed MI. Exponential growth of these fringes first led to primary collapse in cases where the atom number of an individual soliton exceeded a critical value during the early part of MI. The resultant solitons in the train were found to have arbitrary phases. To acquire an alternating-phase structure, it was proposed that a stage of secondary collapses occurred, wherein binary collisions between solitons resulted in annihilations and mergers of near in-phase soliton pairs. These collisions would serve to distill the soliton train, resulting in the eventual formation of alternating phases but accompanied by the loss of a large number of atoms (30).

In a subsequent comparison between MI seeded by noise and self-interference (31), it was determined that both should contribute to MI at comparable timescales. By varying the noise added into their simulations, the authors were able to identify regimes dominated by self-interference or noise. Notably, with MI seeded by self-interference, soliton formation occurred at the edges of the condensate first, since the fringes from self-interference first achieve a sufficiently long wavelength there (30, 31). In contrast, MI seeded by noise led to the development of solitons first in the center, where the density and the rate of MI was highest, and finally at the edges (31).

In the mean-field approaches discussed thus far, the observed stability against secondary collapses is attributed to an alternating-phase structure, although whether this alternating-phase structure is initially present, or evolves out of the mutual annihilation of attractively interacting

solitons has been debated (27–31). Approaches extending beyond mean-field theory, such as the truncated Wigner approximation (TWA) in 1D (32) or the multiconfigurational time-dependent Hartree for bosons (MCTDHB) method (33–35) suggest that quantum effects may produce effectively repulsive interactions, independent of the relative phase. The extension of the TWA to 3D (32), however, resulted in a rapid loss of solitons that contradicts observations (14, 15). Furthermore, convergence with the MCTDHB method has been shown to be pathological for bosons with attractive interactions, which may have affected previous conclusions (36).

We address these issues with a degenerate gas of ${}^7\text{Li}$ atoms. Our methods have been described elsewhere (26, 37). A BEC of atoms in the $|F = 1, m_F = 1\rangle$ state (where F and m_F are the quantum numbers of the total atomic angular momentum and its projection, respectively) is confined in a cylindrically symmetric harmonic trap with radial and axial oscillation frequencies of $\omega_r/2\pi = 346$ Hz and $\omega_z/2\pi = 7.4$ Hz, respectively. The interaction between atoms is magnetically controlled via a broadly tunable Feshbach resonance (38, 39), and is initially set to a scattering length of $a_i \approx 3 a_0$ (where a_0 is the Bohr radius) (37). We quench the interaction to a final scattering length, $a_f < 0$, in a linear ramp time of $t_r = 1$ ms. After waiting a variable hold time, t_h , we take an *in situ* polarization phase-contrast image (PPCI) (40). Our PPCI method can be minimally destructive, resulting in the loss of $< 2\%$ of atoms per image, thus enabling a sequence of images of the same soliton train.

The formation of a soliton train is shown in Fig. 1B for a scattering length of $a_f = -0.18 a_0$, with t_h from 0 to 20 ms (each of these images corresponds to a different experimental run). The images in Fig. 1C depict the formation for a scattering length of $a_f = -2.5 a_0$, highlighting some key differences between smaller and larger $|a_f|$. For larger $|a_f|$ we find that the formation occurs on a faster timescale and we also see a reduction in the number of solitons remaining with increasing t_h . We characterize the effect of MI on the density profile of the BEC by defining a contrast parameter, η , which is a measure of the deviation in the density from a Thomas-Fermi

profile (37). We observe rapid growth of η in the central region as compared with the sides of the condensate (37). According to Ref. 31, this implies that the seed for MI is dominated by noise, which may be technical, thermal, or quantum in origin, rather than self-interference.

The loss of total atom number, N_a vs. t_h , is plotted in Fig. 2A. We observe an initial plateau where N_a changes little, followed by a period of rapid atom loss. The plateau and subsequent atom loss are reminiscent of experiments exploring the collapse of an attractive condensate of ^{85}Rb atoms (41, 42). MI provides a simple and intuitive explanation for this initial plateau. When t_r is fast compared with γ^{-1} , the dynamics are initially frozen out. This timescale is indicated by the arrows in Fig. 2A, calculated for several values of a_f . As $|a_f|$ is increased, γ^{-1} is predicted to become smaller, in agreement with the data. Solitons are formed for times longer than γ^{-1} .

The universality of the MI timescale and of atom loss becomes evident when t_h is rescaled by γ^{-1} (Fig. 2B). We find that the data collapse onto a single curve, with the exception of $a_f = -2.5 a_0$. Because $t_r = 1 \text{ ms} > \gamma^{-1} = 0.42 \text{ ms}$ for this scattering length, the plateau is notably absent. For all other scattering lengths, the onset of atom loss begins shortly after $t_h \gamma = 1$. We fit the data (Fig. 2B) for $t_h > \gamma^{-1}$ to a power law decay, where $N_a = N_0(\gamma t_h)^\kappa$ with $\kappa = -0.35(1)$ (Here N_0 is the total initial number of atoms and κ is the power law exponent).

Scaling laws within the system also provide us with a simple yet surprisingly accurate estimate of the number of solitons, N_s , formed by MI. Assuming an initial condensate length of $2R_{TF}$, where R_{TF} is the Thomas-Fermi radius, we estimate $N_s \simeq 2R_{TF}/(2\pi\xi)$ from simple length scale arguments (27, 29). Because the dynamics of the system are frozen for fast t_r (as compared with γ^{-1}), the initial conditions are entirely determined by $|a_f|$. MI produces a modulation of the density, with the density of defects set by $(2\pi\xi)^{-1}$. In our experiments, R_{TF} is held constant, whereas ξ is controlled by changing a_f . In Fig. 3A we plot N_s vs. a_f , and find excellent agreement with this simple model for $|a_f| < 1 a_0$. For larger $|a_f|$, N_s is limited by

primary collapses that arise when the number of atoms for a single soliton exceeds the critical number for collapse, $N_c = 0.67a_r/|a_f|$, where the factor of 0.67 accounts for the aspect ratio of the trapping potential (16–18). Furthermore, solitons are able to undergo primary collapse during the quench for $t_r > \gamma^{-1}$.

To examine whether primary collapses, or secondary collapses that arise from annihilations or mergers contribute to the observed decrease in N_a , we plot N_s vs. t_h in Fig. 3B. We find that for the two smallest $|a_f|$, $a_f = -0.18 a_0$ and $-0.42 a_0$, N_s remains constant with increasing t_h , indicating that neither primary nor secondary collapses have occurred. The fact that N_s remains constant indicates that the interactions between neighboring solitons are dominantly repulsive, thus suppressing secondary collapses. N_s decreases for larger values of $|a_f|$, indicating the effect of collapse. Because the collisional time scale is expected to be on the order of the breathing mode period, $t_{br} = 68$ ms, we attribute the initial rapid ($t_h < 20$ ms) soliton loss to primary collapses. Secondary collapses are likely to play a role at later times, particularly for the $a_f = -2.5 a_0$ data, for which soliton loss is observed until $N_s \approx 2$. Additional insight into the appearance of collapse may be obtained by examining the strength of the nonlinearity, Δ , which we define as the number of atoms per soliton, normalized to the critical number, $\Delta = N_a/(N_s N_c)$ (Fig. 3C). For both $a_f = -0.18 a_0$ and $-0.42 a_0$ the initial $\Delta < 0.6$, and Δ decays only because of the loss of atoms from each independent soliton, not by losing solitons. On the other hand, the large initial value of Δ for larger $|a_f|$ explains the relative instability to collapse exhibited by these solitons.

To gain further insight into the nature of atom loss, we fit the decay in N_a to a function that assumes that atoms are lost from independent solitons by three-body recombination (Fig. S3). This assumption yields a power law decay, as observed, but with $\kappa = -0.5$ or -0.25 , depending on assumptions regarding the soliton length (37). These values bracket the measured exponent of -0.35 . We extract a three-body loss coefficient, L_3 , from this analysis and find that it ranges

between 10^{-26} and 10^{-25} cm^6/s , depending on the initial assumptions (37). This is much greater than values previously measured for small positive scattering lengths of 10^{-28} cm^6/s (39). Additionally, when the scattering length is ramped slowly (> 250 ms) rather than suddenly quenched, the loss rate is below our ability to measure ($L_3 < 10^{-28}$ cm^6/s) (Fig. S3). We conclude that the much larger rate of loss arises from dynamical changes in the density induced by the sudden quench. One consequence is the excitation of a breathing mode that periodically modulates the density, and thus the rate of three-body loss. The loss rate plateau seen for $t_h > t_{br}/2$ in Fig. 2A is likely a manifestation of this effect. The quench may also induce partial collapses that originate in localized high-density regions of a soliton. The resulting atom loss can self-arrest the collapse, thus resulting in a series of intermittent, partial collapses (43, 44).

Our minimally-destructive imaging technique allows us to take multiple images of the same soliton train to directly observe the dynamics. These images for the small $|a_f|$ data confirm the expected repulsive soliton-soliton interactions. Two such examples are shown for $a_f = -0.18 a_0$ in Figs. 4, A and B. We find that the solitons remain well-separated from one another at *all* times, from which we infer dominantly repulsive interactions, even as the soliton train first emerges.

We have examined MI in detail, elucidating its universal role in the spontaneous formation of matter-wave soliton trains. Our results indicate that MI in this context is driven by noise, and that for small $|a_f|$, neighboring solitons already interact repulsively during the initial formation of the soliton train, independent of secondary collisions. This may also be the case for larger $|a_f|$, but primary collapse dominates the dynamics in this case, and the soliton train quickly dissipates as a result. Similar phase and wavelength correlations have been observed in optical MI experiments (3). We have also demonstrated natural scaling laws for atom loss. The scaling behavior is similar to systems that are described by the Kibble-Zurek mechanism (45–47), although a key difference in our system is the presence of dissipation and collapse, which is

not part of the Kibble-Zurek scenario. The ability to finely control the interaction between atoms, and the relatively slow timescale for dynamics point toward the study of rogue matter-waves (48, 49), analogous to the rogue waves observed in optical systems (50), as a natural extension of this work. Our methods are additionally amenable to studying the formation and propagation of higher-order solitons, such as breathers (51, 52).

Note added in proof: A manuscript reporting modulational instability in ^{85}Rb (53) was posted subsequent to the submission of this manuscript.

References and Notes

1. A. M. Kamchatnov, *Nonlinear periodic waves and their modulations* (World Scientific, 2000).
2. T. B. Benjamin, J. E. Feir, *J. Fluid Mech.* **27**, 417 (1967).
3. D. R. Solli, G. Herink, B. Jalali, C. Ropers, *Nat. Photon.* **6**, 463 (2012).
4. V. E. Zakharov, L. A. Ostrovsky, *Physica D* **238**, 540 (2009).
5. A. Hasegawa, Y. Kodama, *Solitons in optical communications* (Clarendon Press, 1995).
6. P. G. Kevrekidis, D. J. Frantzeskakis, *Mod. Phys. Lett. B* **18**, 173 (2004).
7. N. J. Zabusky, M. D. Kruskal, *Phys. Rev. Lett.* **15**, 240 (1965).
8. V. E. Zakharov, A. B. Shabat, *Sov. Phys.–JETP* **34**, 62 (1972).
9. L. F. Mollenauer, R. H. Stolen, J. P. Gordon, *Phys. Rev. Lett.* **45**, 1095 (1980).
10. A. Hasegawa, *Opt. Lett.* **9**, 288 (1984).
11. K. Tai, A. Hasegawa, A. Tomita, *Phys. Rev. Lett.* **56**, 135 (1986).

12. Z. Chen, M. Segev, D. N. Christodoulides, *Rep. Prog. Phys.* **75**, 086401 (2012).
13. L. Khaykovich *et al.*, *Science* **296**, 1290 (2002).
14. K. E. Strecker, G. Partridge, A. G. Truscott, R. G. Hulet, *Nature* **417**, 150 (2002).
15. S. L. Cornish, S. T. Thompson, C. E. Wieman, *Phys. Rev. Lett.* **96**, 170401 (2006).
16. V. M. Pérez-García, H. Michinel, H. Herrero, *Phys. Rev. A* **57**, 3837 (1998).
17. A. Gammal, T. Frederico, L. Tomio, *Phys. Rev. A* **64**, 055602 (2001).
18. N. G. Parker, S. L. Cornish, C. S. Adams, A. M. Martin, *J. Phys. B: At., Mol. Opt. Phys.* **40**, 3127 (2007).
19. J. P. Gordon, *Opt. Lett.* **8**, 596 (1983).
20. F. M. Mitschke, L. F. Mollenauer, *Opt. Lett.* **12**, 355 (1987).
21. J. S. Aitchison *et al.*, *Opt. Lett.* **16**, 15 (1991).
22. B. B. Baizakov, B. A. Malomed, M. Salerno, *Phys. Rev. A* **70**, 053613 (2004).
23. L. Khaykovich, B. A. Malomed, *Phys. Rev. A* **74**, 023607 (2006).
24. N. G. Parker, A. M. Martin, S. L. Cornish, C. S. Adams, *J. Phys. B: At., Mol. Opt. Phys.* **41**, 045303 (2008).
25. N. G. Parker, A. M. Martin, C. S. Adams, S. L. Cornish, *Physica D* **238**, 1456 (2009).
26. J. H. V. Nguyen, P. Dyke, D. Luo, B. A. Malomed, R. G. Hulet, *Nat. Phys.* **10**, 918 (2014).
27. U. Al Khawaja, H. T. C. Stoof, R. G. Hulet, K. E. Strecker, G. B. Partridge, *Phys. Rev. Lett.* **89**, 200404 (2002).

28. L. Salasnich, A. Parola, L. Reatto, *Phys. Rev. A* **66**, 043603 (2002).
29. L. Salasnich, A. Parola, L. Reatto, *Phys. Rev. Lett.* **91**, 080405 (2003).
30. L. D. Carr, J. Brand, *Phys. Rev. Lett.* **92**, 040401 (2004).
31. L. D. Carr, J. Brand, *Phys. Rev. A* **70**, 033607 (2004).
32. B. J. Dąbrowska-Wüster, S. Wüster, M. J. Davis, *New J. Phys.* **11**, 053017 (2009).
33. A. I. Streltsov, O. E. Alon, L. S. Cederbaum, *Phys. Rev. Lett.* **106**, 240401 (2011).
34. A. I. Streltsov, O. E. Alon, L. S. Cederbaum, *Phys. Rev. Lett.* **100**, 130401 (2008).
35. K. Sakmann, M. Kasevich, *Nat. Phys.* **12**, 451 (2016).
36. J. G. Cosme, C. Weiss, J. Brand, *Phys. Rev. A* **94**, 043603 (2016).
37. See the supplementary materials on Science Online.
38. S. E. Pollack *et al.*, *Phys. Rev. Lett.* **102**, 090402 (2009).
39. P. Dyke, S. E. Pollack, R. G. Hulet, *Phys. Rev. A* **88**, 023625 (2013).
40. C. C. Bradley, C. A. Sackett, R. G. Hulet, *Phys. Rev. Lett.* **78**, 985 (1997).
41. E. A. Donley *et al.*, *Nature* **412**, 295 (2001).
42. P. A. Altin *et al.*, *Phys. Rev. A* **84**, 033632 (2011).
43. Yu. Kagan, A. E. Muryshev, G. V. Shlyapnikov, *Phys. Rev. Lett.* **81**, 933 (1998).
44. H. Saito, M. Ueda, *Phys. Rev. Lett.* **86**, 1406 (2001).
45. T. W. B. Kibble, *J. Phys. A—Math Gen.* **9**, 1387 (1976).

46. W. H. Zurek, *Nature* **317**, 505 (1985).
47. A. Polkovnikov, K. Sengupta, A. Silva, M. Vengalattore, *Rev. Mod. Phys.* **83**, 863 (2011).
48. Yu. V. Bludov, V. V. Konotop, N. Akhmediev, *Phys. Rev. A* **80**, 033610 (2009).
49. L. Wen *et al.*, *Eur. Phys. J. D* **64**, 473 (2011).
50. D. R. Solli, C. Ropers, P. Koonath, B. Jalali, *Nature* **450**, 1054 (2007).
51. P. G. Kevrekidis, G. Theocharis, D. J. Frantzeskakis, B. A. Malomed, *Phys. Rev. Lett.* **90**, 230401 (2003).
52. H. Sakaguchi, B. A. Malomed, *Phys. Rev. E* **70**, 066613 (2004).
53. P. J. Everitt *et al.*, *arXiv:1703.07502* (2017).
54. We thank K. Hazzard, L. Carr, E. Mueller, and B. Malomed for helpful discussions. This work was supported by the NSF (Grants PHY-1408309 and PHY-1607215), the Welch Foundation (Grant No. C-1133), an ARO-MURI (Grant No. W911NF-14-1-0003) and the ONR.

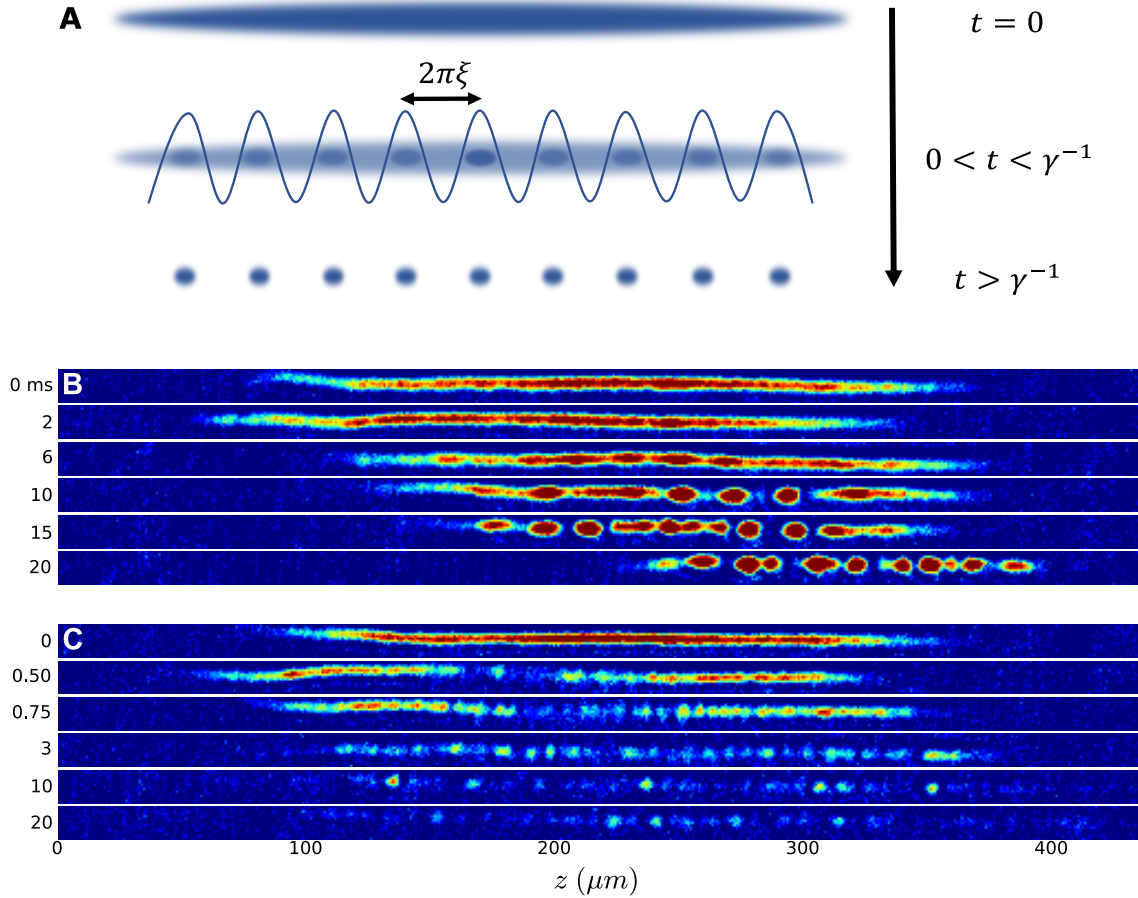


Fig. 1. Soliton train formation from modulational instability (MI). (A) Schematic representation of the effects of a scattering length quench. At short times, the condensate has not responded to changes in scattering length. MI results in rapid growth of fluctuations at a length scale of $2\pi\xi$. Atoms flow towards regions of high density on a timescale of γ^{-1} owing to a nonlinear focusing from attractive interactions. Solitons are formed for $t > \gamma^{-1}$. (B) Column density images for $a_f = -0.18 a_0$. Immediately after the quench, there is no discernible change in N_a , nor is there any change in the shape from that of the original condensate at $a_i = +3 a_0$. Solitons form at later times, and undergo breathing and dipole oscillations. (C) Similar to B, except with $a_f = -2.5 a_0$. Modulations appear much earlier, as do gaps near the center where the density of the original condensate was high, which we attribute to primary collapses. A reduction in N_s is evident at longer t_h . Each image corresponds to a different experimental run, and hence real-time dynamics cannot be directly inferred from these images. Here, z is the position along the axial coordinate.

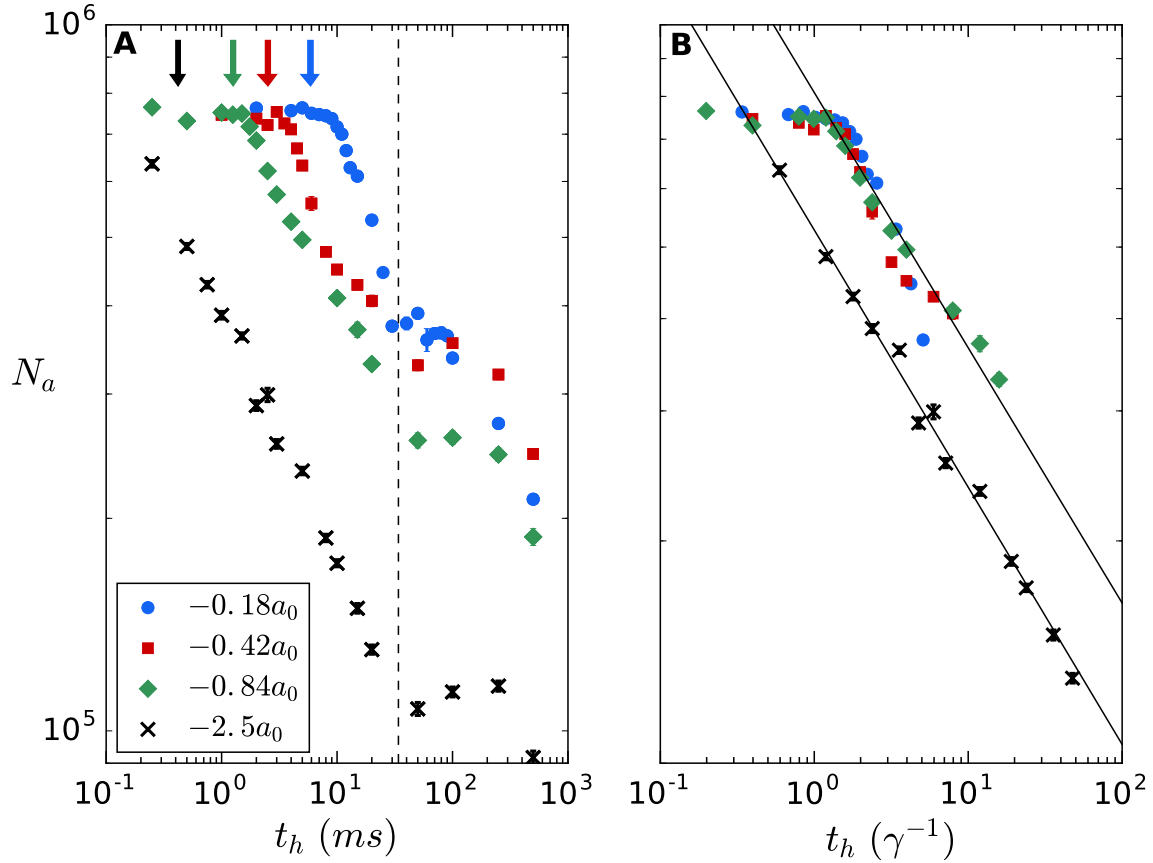


Fig. 2. Post-quench evolution of atom number. (A) N_a vs. t_h for various a_f . The arrows indicate the calculated γ^{-1} for each value of a_f , which is determined using the peak value of n_{1D} . The black dashed line corresponds to half of a breathing period ($t_{br} = 68$ ms). We observe a plateau in N_a for each a_f , followed by a rapid decrease in atoms starting shortly after $t_h \approx \gamma^{-1}$. We attribute the lack of a plateau for $a_f = -2.5 a_0$ to $t_r > \gamma^{-1}$. (B) Data replotted vs. $t_h \gamma$. The data collapse onto a single curve, except for $a_f = -2.5 a_0$. The data are fit to a power law, $N_a = N_0(t_h \gamma)^{\kappa}$, shown as a solid black line, where $\kappa = -0.35(1)$ for both fits. For all a_f , points for $t_h > t_{br}/2$ have been omitted from the fit. Error bars are the standard deviation of the mean of up to 30 shots.

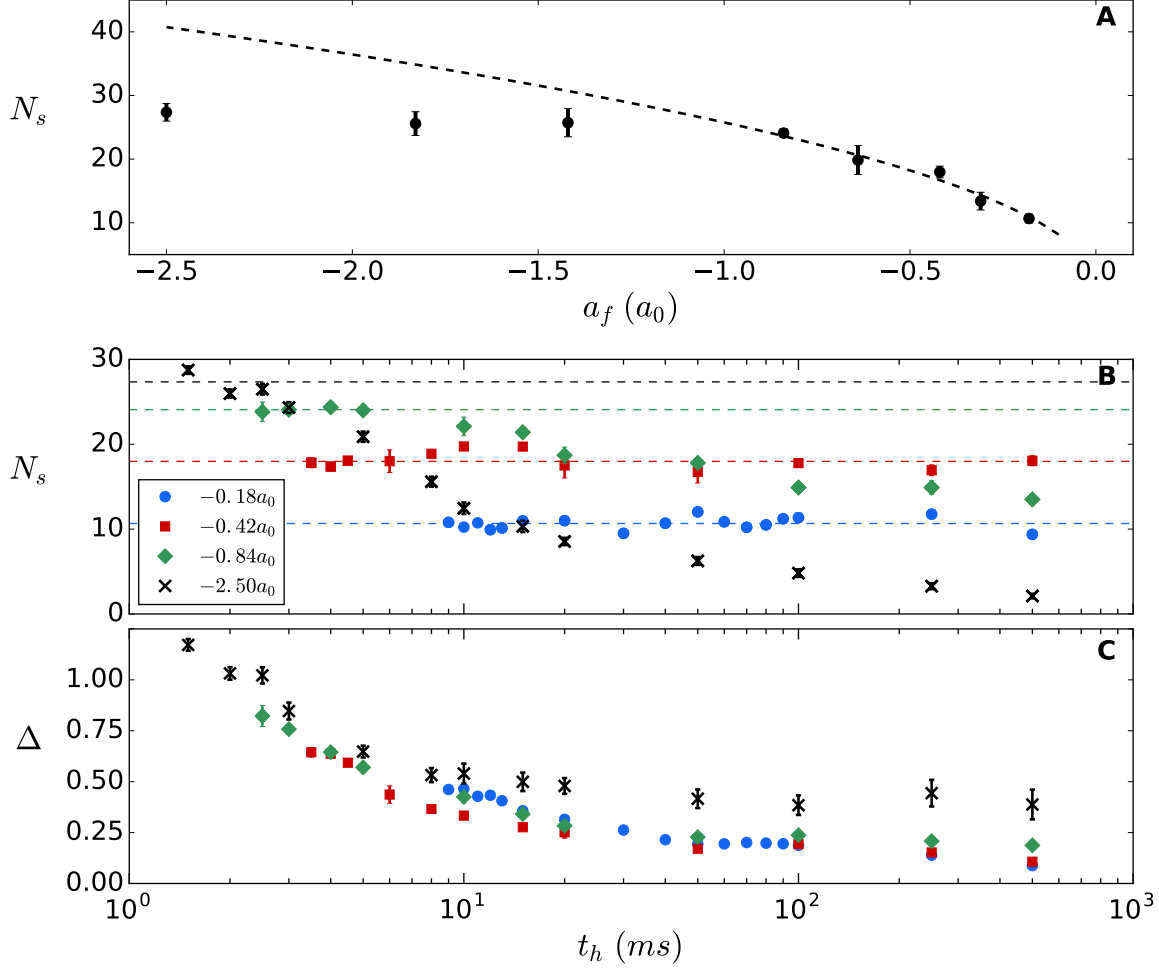


Fig. 3. Post-quench evolution of soliton number and strength of nonlinearity. (A) N_s vs. a_f . The dashed line corresponds to a fit of the data to the model (see text), where an overall scaling of $1.04(2)$ is the only fit parameter. Data for $|a_f| > 1 a_0$ are omitted from the fit. We attribute the suppression in N_s for $|a_f| > 1 a_0$ to primary collapse, resulting in a reduction in the number of solitons formed. (B) N_s vs. t_h . N_s does not change with t_h for the two smallest $|a_f|$, whereas for larger $|a_f|$, N_s decays with t_h . Dashed lines correspond to the initial number of solitons. (C) Δ vs. t_h . The initial value of $\Delta = N_a/(N_s N_c)$ increases as $|a_f|$ is increased, and is consistent with an expected $\sqrt{|a_f|}$ scaling. This trend continues up to $\Delta = 1$, above which the solitons are unstable against primary collapse. Error bars are the standard deviation of the mean of up to 30 shots.

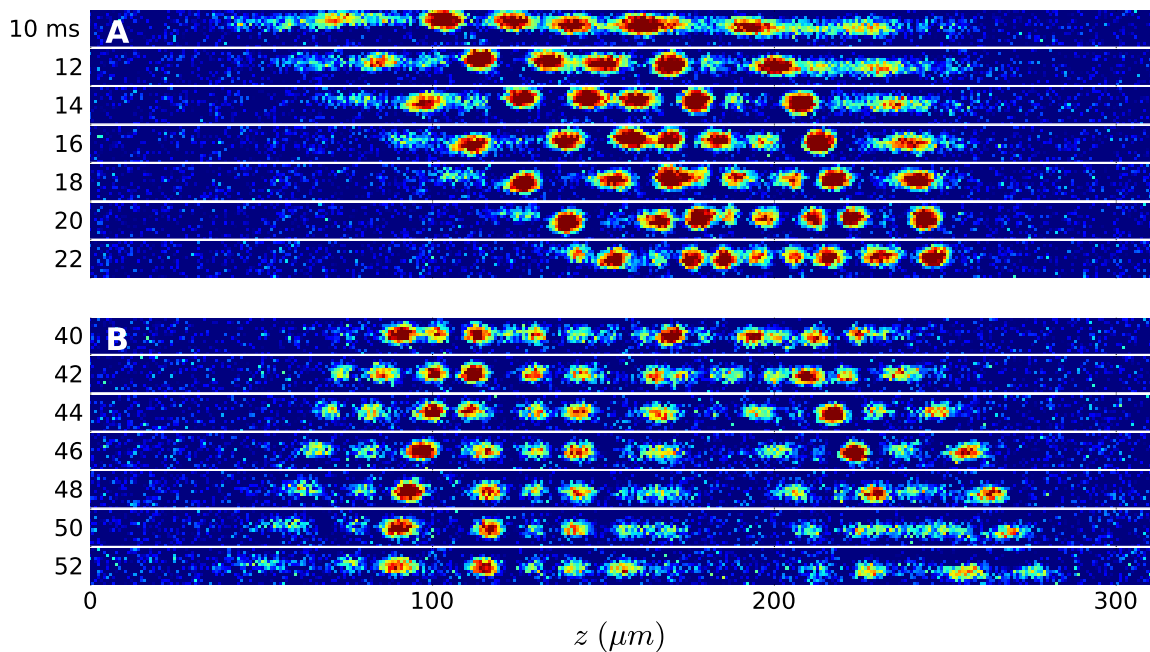


Fig. 4. Soliton train dynamics. (A) Multiple images of the same soliton train, for $a_f = -0.18 a_0$. Beginning at $t_h = 10$ ms, a new image was taken every 2 ms. We infer dominantly repulsive interactions although occasional attractive collisions occur between neighbors. The reduction in the overall size of the train is caused by a breathing mode excited by the quench, and a dipole oscillation is also evident. (B) Similar to A, starting with $t_h = 40$ ms. The effects of the breathing mode in its expansion phase are evident.

Supplementary Materials for Formation of matter-wave soliton trains by modulational instability

Jason H.V. Nguyen, De Luo, and Randall G. Hulet

Department of Physics and Astronomy, Rice University, Houston TX, 77005, USA

correspondence to: randy@rice.edu

This PDF includes:

Materials and Methods

Supplementary Text

Fig. S1

Fig. S2

Fig. S3

Materials and Methods

Experimental Methods

The apparatus used here has been described previously (26). The harmonic trapping potential is derived from a laser beam operating at 1070 nm, directed parallel to the magnetic field axis, and focused at the atoms to a $1/e^2$ radius of 32 μm , giving us radial and axial trapping frequencies of $\omega_r/2\pi = 346$ Hz and $\omega_z/2\pi = 7.4$ Hz, respectively.

A pair of coils in the Helmholtz configuration is used to create a uniform magnetic field along the z-axis. The scattering length may be tuned across a broad region via the Feshbach resonance located at 738 G (38,39). Initially, a BEC is formed at a field of 716 G, corresponding to a scattering length of $a \approx 140 a_0$. The field is ramped in 250 ms to a field of 565 G where $a \approx 3 a_0$, corresponding to the initial conditions of all of our experiments. We find that a ramp time of 250 ms is sufficiently slow that no breathing mode is excited. At this point, the field is quenched ($t_r = 1$ ms) to a final scattering length of $-2.5 a_0 < a_f < -0.18 a_0$. Within ± 4 G of the zero-crossing at 543.6(1) G, the scattering length follows a linear relationship with a slope of 0.08(1) a_0/G (39).

To determine N_a , N_s , and Δ , an *in situ* image of the atoms is taken using polarization phase contrast imaging (40), with the laser detuned from resonance by 20Γ , where $\Gamma = 5.9$ MHz is the natural linewidth of ${}^7\text{Li}$. In order to examine the dynamics within a given experimental run, the imaging laser was detuned from resonance by 50Γ , which afforded a good signal to noise ratio while keeping the atom loss below 2% per image. N_a is determined by integrating the column density image. N_s is determined using a peak finding algorithm which subsequently fits the data to N_s Gaussians, and from the fits we determine the separation between solitons, their $1/e$ axial length, and the total number of atoms in each soliton, which agrees to within 10% of the number determined by doubly-integrating the image. For each data point in Figs. 2 and 3, we

take up to 30 averages, with error bars representing the standard deviation of the mean.

Supplementary Text

Calculation of η

To determine the effect of MI on the density of condensate, we integrate our images along the radial direction in order to obtain a line density, as shown in Fig. S1. The data is subsequently fit to a Thomas-Fermi distribution:

$$n(z) = \begin{cases} n_p \beta^2 + b, & \beta > 0 \\ b, & \beta < 0 \end{cases} \quad (\text{S1})$$

where $\beta = 1 - \left(\frac{z-z_0}{z_{TF}}\right)^2$. We define a contrast parameter as:

$$\eta = \frac{\sqrt{\sum_i (n_e(i) - n_f(i))^2}}{n_p}, \quad (\text{S2})$$

where $n_e(i)$ corresponds to the experimentally obtained line density at point i , and $n_f(i)$ is the obtained from the fit of the data at point i . We split the condensate into equal thirds, and calculate η_L for the left-most region, η_C for the central region, and η_R for the right-most region. In Fig. S2 we plot η vs. t_h for $a_f = -0.18 a_0$. We observe a rapid growth of η_C as compared to η_R and η_L , which we interpret as evidence that MI is predominantly seeded in the center of the distribution, and hence by noise, rather than by self-interference.

Determination of the three-body decay rate

The decay in atom number resulting from three-body recombination can be analytically determined from:

$$\frac{1}{N_a} \frac{dN_a}{dt} = -\frac{L_3}{6} \langle n^2 \rangle, \quad (\text{S3})$$

where L_3 is the three-body loss coefficient, and $\langle n^2 \rangle$ is the spatially-averaged second moment of the density. For simplicity, we determine the decay rate for a single soliton, and we consider

two separate cases. First, we assume that the density is well-described by the ground state of a harmonic oscillator, and thus the density is:

$$n(r, z) = \frac{N_a}{\pi^{3/2} a_r^2 a_z} e^{[-(r/a_r)^2]} e^{[-(z/a_z)^2]}, \quad (\text{S4})$$

where $a_{r,z} = \sqrt{\hbar/(m\omega_{r,z})}$ is the harmonic oscillator length along the radial and axial directions, respectively. Using Eq. S4 we obtain:

$$\langle n^2 \rangle = \frac{N_a^2}{3\sqrt{3}\pi^3 a_r^4 a_z^2}, \quad (\text{S5})$$

and using this we can solve Eq. S3, resulting in:

$$N_a(t_h) = \frac{N_0}{\left[\frac{L_3 N_0^2}{9\sqrt{3}\pi^3 a_r^4 a_z^2} t_h + 1 \right]^{1/2}}, \quad (\text{S6})$$

where N_0 is the initial atom number.

In obtaining Eq. S6 we have implicitly assumed that the length of the soliton is constant. In fact, the density may be more accurately described using the number-dependent wavefunction of a soliton:

$$n(r, z) = \frac{N_a}{4\pi a_r^2 \xi} e^{[-(r/a_r)^2]} \text{sech}^2 \left(\frac{z}{2\xi} \right), \quad (\text{S7})$$

where $\xi = \hbar^2/(m|g_{1D}|N_a)$ and $g_{1D} = 2\hbar\omega_r a$. Here, the axial length of the soliton changes as with changing N_a . In this case, the second moment of the density is given by:

$$\langle n^2 \rangle = \frac{m^2 g_{1D}^2}{90\pi^2 a_r^4 \hbar^4} N_a^4, \quad (\text{S8})$$

and when this is used to solve Eq. S3 we obtain:

$$N_a(t_h) = \frac{N_0}{\left[\frac{m^2 g_{1D}^2 L_3 N_0^4}{135\pi^2 a_r^4 \hbar^4} t_h + 1 \right]^{1/4}}, \quad (\text{S9})$$

The power law behavior $N_a \propto t_h^{-1/2}$ for a fixed length, or $N_a \propto t_h^{-1/4}$ for a time-varying one brackets our fitted decay exponent of $\kappa = -0.35(1)$. We fit our data to Eqs. (S6) and

(S9) to determine L_3 (see Fig. S3). We assume that each soliton can be treated independently, and so we only fit the data for $a_f = -0.18 a_0$ where $N_s \approx 11$ and $a_f = -0.42 a_0$ where $N_s \approx 18$. For both scattering lengths, we only include data starting when we see a decrease in atom number, and up to $t_h = t_{br}/2$ (indicated by the dashed vertical line). We obtain a value of $L_3 \sim 10^{-26} \text{ cm}^6/\text{s}$ for $a_f = -0.18 a_0$ and $L_3 \sim 10^{-25} \text{ cm}^6/\text{s}$ for $a_f = -0.42 a_0$. In contrast, we find that when we slowly ramp the scattering length ($t_r = 500 \text{ ms}$) to $a_f = -0.18 a_0$, $N_s \approx 2$, and the atom number remains relatively flat, even though the initial number of atoms per soliton is similar to the quench data for $a_f = -0.18 a_0$. From this, we are able to set an upper limit of $L_3 < 10^{-28} \text{ cm}^6/\text{s}$. We conclude that our extracted values of L_3 arise from an enhancement of the density, either by the induced breathing mode, or partial collapses due to the quench.

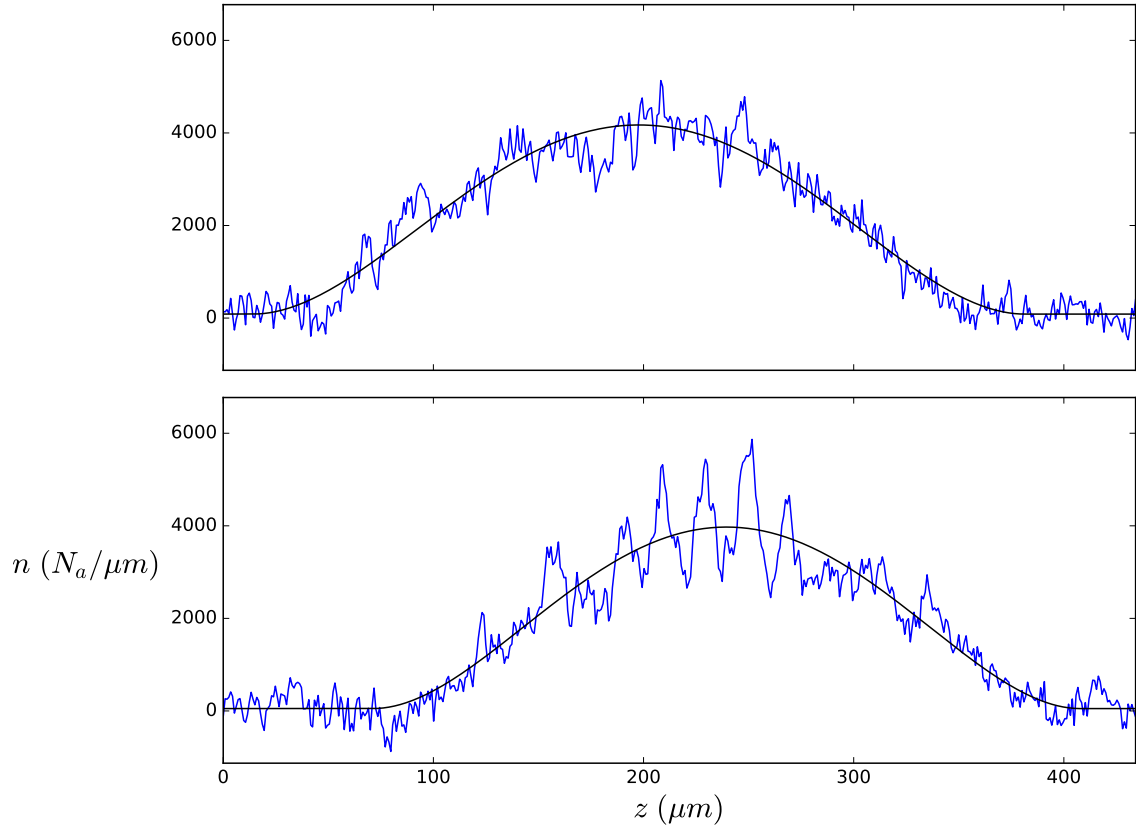


Fig. S1. Representative Line density. (A) Line density for $t_h = 2$ ms and $a_f = -0.18 a_0$. The black solid line corresponds to fitting the data to Eq. 1. (B) Similar to (A) but with $t_h = 6$ ms.

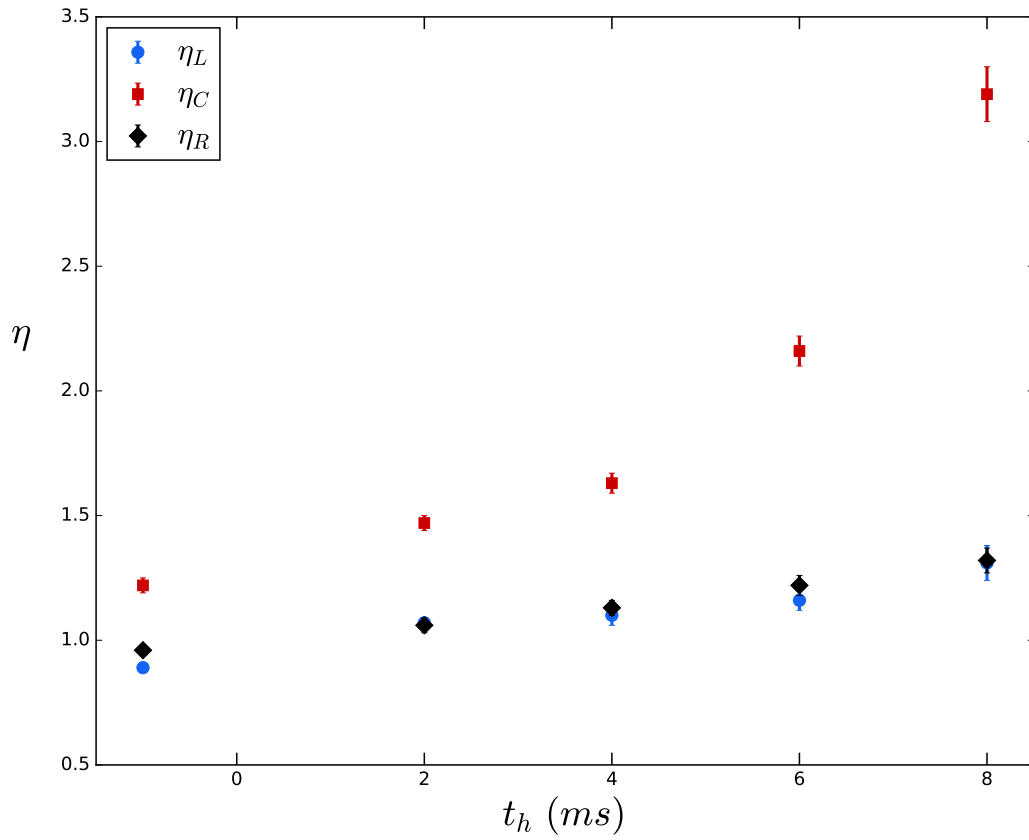


Fig. S2. Onset of MI at early times. η vs. t_h for $a_f = -0.18 a_0$. We observe a rapid growth in η_C as compared to η_L and η_R . Each point corresponds to an average of up to 30 experimental runs.

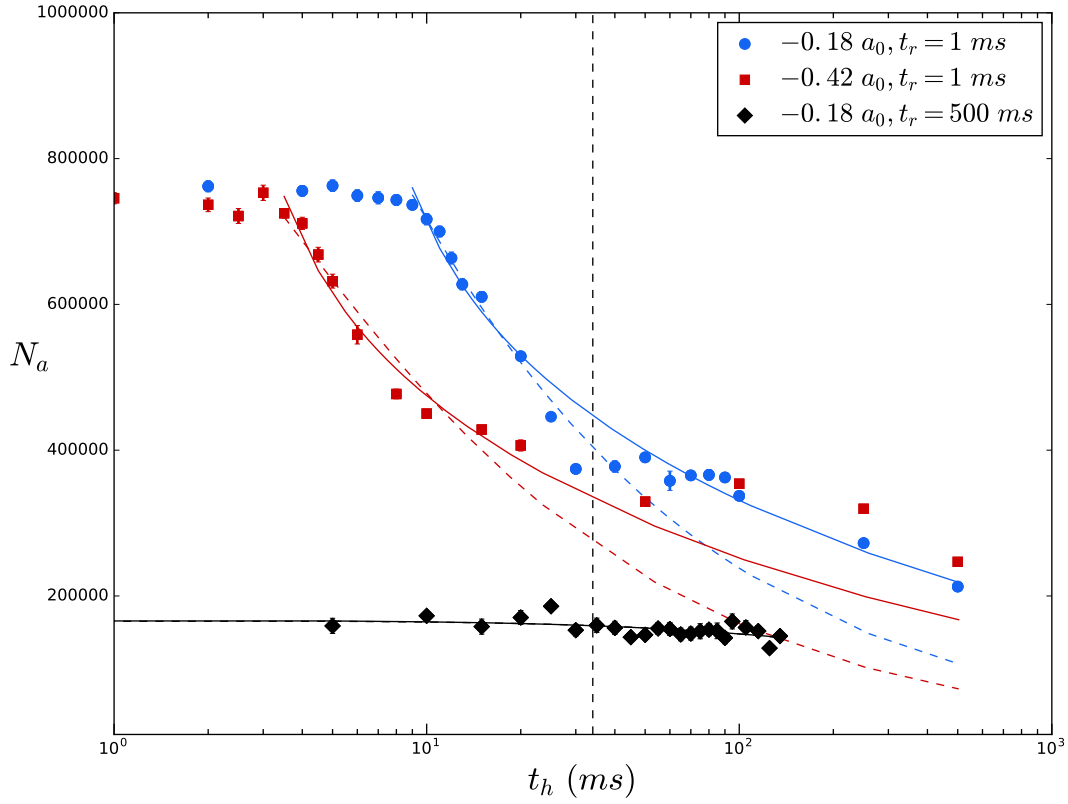


Fig. S3. Fit to obtain three-body loss coefficient. N_a vs. t_h . The dashed lines corresponds to assuming a fixed soliton axial length while solid lines corresponds to allowing the soliton length to increase with decreasing number. For the slow ramp data (black) we are unable to detect atom loss for t_h up to 100 ms.